Imaging phase-separated domains in conducting polymer blend films with near-field scanning optical microscopy

Jeeseong Hwang, Lori S. Goldner, Alamgir Karim, and Connie Gettinger

We present high-resolution images with near-field scanning optical microscopy to study phase separation in polymer films of poly(styrene) and poly(3-octyl-thiophene). Transmission and transmitted fluorescence near-field scanning optical microscope images were taken for direct visualization of the intermediate steps of phase separation in a regime where small domain sizes prevent investigation by conventional microscopy. The interpretation of near-field data on samples with large or varying film thickness or topography are also discussed, and a method for recognizing topographically induced artifacts in a quantitative way is suggested. © 2001 Optical Society of America

OCIS codes: 180.5810, 160.5470, 240.5770, 310.3840.

1. Introduction

Conventional methods to fabricate small structures and patterns employ mainly high-resolution lithographic techniques that are time consuming and expensive. More recently, innovative techniques involving control and use of the molecular microenvironment in polymer blends have drawn attention for generating submicrometer patterns.[1,2] Among those techniques, phase-separation-induced assembly of surface patterns in thin polymer blend films is being investigated.[3,4] The understanding of electrical, mechanical, and optical properties of conducting polymer blends has been a subject of increasing importance in light of growing efforts to adopt the use of blends in device fabrication.[5] Moreover, there is an increased need to characterize these properties with nanoscale resolution as organic optoelectronic devices are fabricated on an ever smaller length scale. Near-field scanning optical microscopy (NSOM) provides a technique for the optical and topographic characterization of thin-film blends with optical resolution significantly better than what can be achieved in ordinary microscopy. In NSOM a small light source is used as a scanning probe to map the optical properties of a system with resolution that depends on the size of the light source and the distance between the source and the sample.[6] In the instruments used here the light source is a small aperture at the end of a sharpened and aluminum-coated optical fiber.[7] Most of the contrast mechanisms in far-field microscopy such as transmission and fluorescence can be adopted in NSOM. Topographic images are simultaneously acquired as a result of the feedback mechanism required for maintaining the tip close to the sample surface. This makes NSOM a unique optical technique to map the dynamics of phase-separating polymer blends by correlation of changes in morphology with local variations in composition in multicomponent polymer films.

NSOM has been successfully applied to the study of several monomolecular polymeric samples. Thin films of various conjugate polymers were investigated by NSOM to resolve localized mesoscale aggregates in poly(p-pyridyl vinylene)[8] and molecular orientations in the domains of poly(p-phenylene vinylene) (PPV) films.[9] Local optical absorption of a bilayer film of tris(8-hydroxy)quinoline aluminum/PPV was also investigated by NSOM in transmission and reflection modes.[10] In this paper we study the phase dynamics of polymer samples with significant roughness, and we report on the limitations of NSOM when

J. Hwang (jch@nist.gov) and L. S. Goldner are with the Optical Technology Division, Physics Laboratory, National Institute of Standards and Technology, Gaithersburg, Maryland 20899. A. Karim is with the Polymers Division, Materials Science and Engineering Laboratory, National Institute of Standards and Technology, Gaithersburg, Maryland 20899. C. Gettinger is with the Corporate Processing Technology Center, 3M Company, St. Paul, Minnesota 55144.

Received 22 January 2001; revised manuscript received 1 May 2001.

0003-6935/01/223737-09$15.00/0

used on rough samples. The samples are binary polymer blend films in which one of the polymer components is conducting; samples are thin films of a poly(3-octyl-thiophene) (POT)/poly(styrene) (PS) blend deposited onto bare borosilicate glass substrates. Electrically conducting POT is of commercial interest because of its environmental stability and excellent processibility both in solution and in the melt, which enables reliable production of ultrathin films by spin casting or quenching to an intermediate stage of phase-separating morphology. Photoexcitation of POT results in a broadband luminescence with the absorption and the emission peak at 440 and 525 nm, respectively.[11] Therefore fluorescence contrast can be used in NSOM to map the distribution of the POT-rich phase in the blend.

2. Experiment

A. Materials

PS with nominal molecular mass[12] $M_W = 96{,}000$ and glass transition temperature of 110 °C was purchased from the Toyo Soda Manufacturing Company. POT was prepared according to the procedures described in the literature.[13] The M_W of POT measured by gel permeation chromatography was 10,000.

B. Sample Preparation

Samples consisted of thin films of a POT/PS blend deposited on glass substrates. The films were prepared by spin casting from a dilute mixture of the blend in toluene. The substrates were 18-mm-diameter round borosilicate #1 cover glasses purchased from Thomas Scientific. The cover glasses were cleaned with a solution of H_2SO_4:H_2O_2 = 3:1 (volume ratio) mixture for 2 h and washed thoroughly with deionized water. The initial cleaning procedure was followed by boiling the substrates in 0.5% (volume fraction) detergent solution, cleaning with pure methanol, and baking overnight between 150 and 170 °C in a convection oven. To study phase-separation dynamics, samples annealed at different temperatures were stored in a temperature-regulated vacuum oven for a desired time period, taken out to cool down in an ambient condition, and imaged with NSOM or far-field fluorescence microscopy at room temperature.

C. Optical Microscopy

Conventional epifluorescence microscopy was used for imaging samples with a xenon arc lamp and a triple-filter set XF25 (excitation filter, Model 485DF22; dichroic beam splitter, Model 505DRLP02; emission filter, Model OG530) by Omega Optical. The triple-filter set was mounted in the fluorescence filter cube of an optical microscope (Zeiss Axiovert TV 135).

D. Near-field Scanning Optical Microscopy

Near-field scanning microscopy was carried out with home-built NSOM heads combined with optical microscopes. The NSOMs use a straight, aluminum-coated tapered single-mode optical fiber tip, controlled by either an optical or a mechanical feedback mechanism, to monitor and regulate tip–sample distance.[14,15] In these experiments 488-nm light is emitted from the NSOM fiber tip. The sample is held within the near field of the tip and scanned above the tip to form an image. Light emitted from or passing through the sample was collected with various objective lenses (40×, 0.75 N.A.; 100×, 1.25 N.A.). All the NSOM images were taken with a 1.25-N.A. objective except for the unannealed sample. Two instruments were used, and details of their construction and schematics can be found elsewhere.[16,17] The signal was split into fluorescent and transmitted components with a dichroic beam splitter with a passband of 488 nm ± 5 nm. Several detectors were used, but typically an avalanche photodiode (EG&G Model PQ-200) was used to count fluorescent photons, and a small-area silicon photodiode was used to monitor the transmitted signal. An RHK scanning tunnel microscope STM 1000 system was used for controlling the instruments and acquiring data. A data-acquisition board, National Instruments Model DT2821, and pulse counting board, National Instruments Model PCTIO10, were used for digital construction of topographic data, transmission, and fluorescence optical images at the same time.

E. Image Processing for Two-Dimensional Autocorrelation

The two-dimensional (2D) autocorrelation function of a topographic image was calculated as $g(\boldsymbol{\xi}) = g(\xi_x, \xi_y) = [\langle p(\mathbf{r})p(\mathbf{r} + \boldsymbol{\xi})\rangle - \langle p(\mathbf{r})\rangle^2]/\langle p(\mathbf{r})\rangle$,[2] where $\boldsymbol{\xi}$ is the spatial lag vector, $\langle\ \rangle$ is the average over the entire image, and $p(\mathbf{r})$ is a pixel value at each point $\mathbf{r}$. The averaged autocorrelation term in the denominator was obtained with a 2D fast-Fourier-transform algorithm; the original image was Fourier transformed to obtain its 2D power-spectrum matrix, and the matrix was then inversely Fourier transformed again.[18] We obtained the angle-averaged autocorrelation function, $g(|\boldsymbol{\xi}|)$, by averaging over all angles of the spatial lag vector $\boldsymbol{\xi}$, keeping the length of $\boldsymbol{\xi}$, $|\boldsymbol{\xi}|$ fixed. All the image-processing calculations were performed with the fast-Fourier transform and other algorithms of interactive data language image-processing software.

3. Results and Discussion

For the initial characterization of the films, far-field fluorescence microscopy was used to obtain images for the following as-cast PS:POT film samples of 0.5% mass fraction in toluene: (i) 1:1 (mole ratio) blend spin cast at 84 rad/s [800 revolutions per minute (rpm)], (ii) 1:1 (mole ratio) blend spin cast at 314 rad/s (3000 rpm), (iii) 2:1 (mole ratio) blend spin cast at 84 rad/s (800 rpm), and (iv) 2:1 (mole ratio) blend spin cast at 314 rad/s (3000 rpm). Average thickness of the samples cast at 314 rad/s (3000 rpm) and 84 rad/s (800 rpm) was estimated to be 40 and 80 nm respectively.[19] Far-field fluorescence images on these samples exhibiting domain structures are displayed in Fig. 1. We took the displayed images ap-

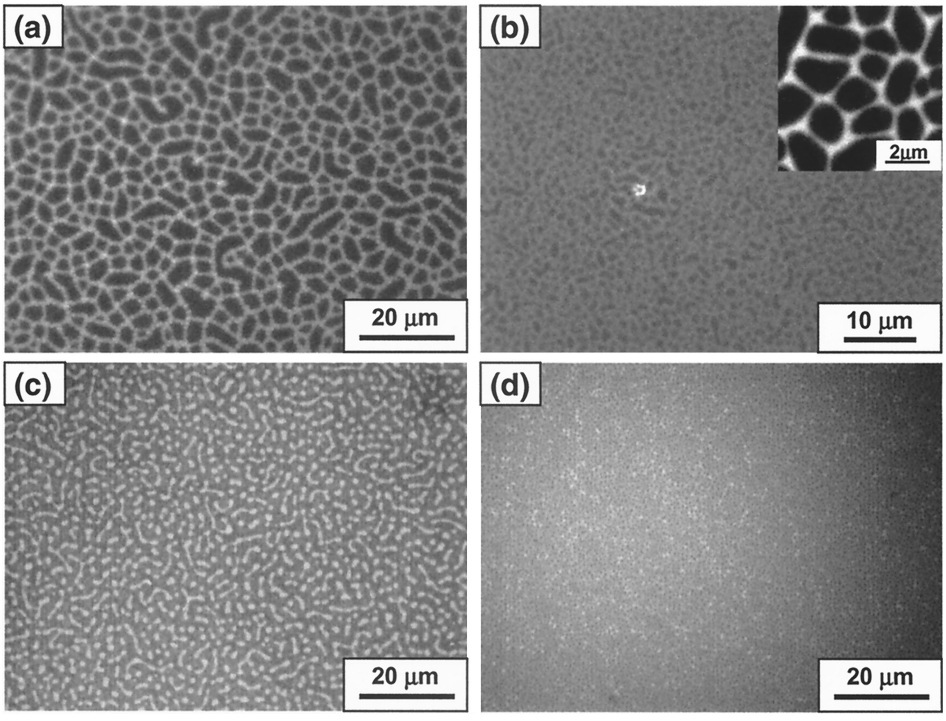

Fig. 1. Fluorescence images of unannealed samples taken in far-field fluorescence microscopy. (a) PS:POT = 1:1 cast at 84 rad/s (800 rpm). (b) Same blend cast 314 rad/s (3000 rpm). Inset, fluorescence near-field image of the same sample. (c) PS:POT = 2:1 cast at 84 rad/s (800 rpm). (d) Same blend cast at 314 rad/s (3000 rpm). We used 40×, 0.75-N.A. objective for (a), (c), and (d) and 100×; 1.25 N.A. for (b).

proximately 1 h after the spin casting, and we found no significant change in the samples even after several weeks. The 1:1 blend samples prepared either at 84 rad/s (800 rpm) [(Fig. 1(a)] or at 314 rad/s (3000 rpm) [Fig. 1(b)] showed a fluorescent network pattern formed by the POT-rich phase, indicative of a percolating conductive cellular network. From these far-field images some qualitative comparisons between thick and thin samples were possible. For instance, in thinner samples cast at higher rpm, the size of polygons bounded by fluorescent lines became smaller than in the thicker sample, and the fluorescence contrast decreased with film thickness. For both blends the thicker films [Figs. 1(a) and 1(c)] show a contrast approximately twice that of the thin samples [Figs. 1(b) and 1(d)], which is consistent with the estimated thicknesses. In addition, the thicker sample [Fig. 1(a)] showed slight evidence of round droplets in POT-rich domains; in the thinner films the presence or the absence of these droplets cannot be ascertained with only far-field techniques [Fig. 1(b)]. A near-field image of the thin film, however, showed no evidence for droplet formation in the sample of Fig. 1(b) [see inset of Fig. 1(b)]. In thicker films the drying process by solvent evaporation is slow, probably permitting the formation of round subdomains by means of a Rayleigh instability.

Domain shape changed significantly when composition ratio of the blend was altered. Far-field fluorescence images of PS:POT = 2:1 blend films cast at 84 rad/s (800 rpm) showed features large enough to be resolved with far-field microscopy. The features were a mixture of "wormy" and round fluorescent domains apparently similar to the characteristics of spinodal decomposition [Fig. 1(c)].[20] In contrast to previous 1:1 blend samples, these individual fluorescent domains did not appear to be percolating. Thinner films cast at higher speed appeared nearly homogeneous in the far field, with barely resolvable isolated dark and fluorescent patches [Fig. 1(d)] indicative of domain formation by nucleation process. However, near-field images of this same sample revealed a percolating network of POT-rich domains suggesting a more complex mechanism (Fig. 2, discussed below).

Figure 2 shows near-field images of the sample of Fig. 1(d). Although many features were too fine to be resolved with far-field microscopy, NSOM images clearly revealed the details of the domain structure in this sample. Histogram analysis of topographic NSOM images showed that the sample contained depressed domains approximately 5 nm ± 2 nm (standard deviation) lower on average, seen as dark patches in a topographic image [see arrows j_1 and j_2 in Figs. 2(a) and 2(d)]. Corresponding NSOM optical images, taken both in transmission (488 nm) and transmitted fluorescence (515 nm and above) contained additional compositional information. The transmission images [Figs. 2(b) and 2(e)] seem to indicate that the absorbing regions, presumably POT rich, are droplet shaped and localized at the depressions in the film. The fluorescence images [Figs. 2(c)

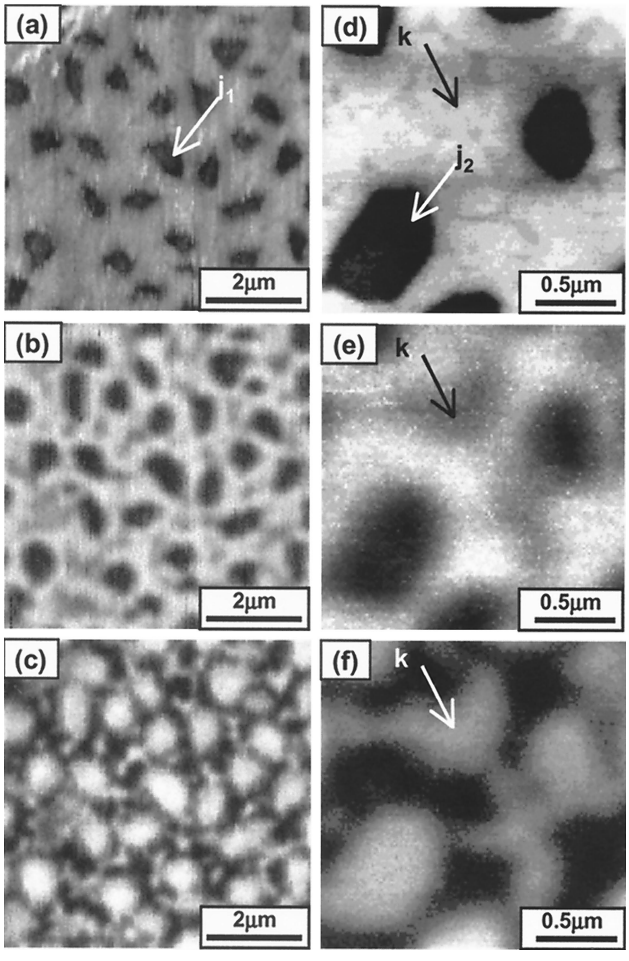

Fig. 2. Near-field images of an unannealed sample of PS:POT = 2:1 mixture cast at 314 rad/s (3000 rpm): (a) topography, (b) transmission of the excitation light at 488 nm, (c) fluorescence emission from POT. Near-field images for a smaller scan area: (d) topography, (e) transmission, (f) fluorescence. Arrows indicate POT-rich domain located at a depression in the topography.

and 2(f)] tell a more detailed story and in fact give evidence for a percolating network of POT in this as-cast film that is also recognizable in transmission only after inspection of the fluorescence images [compare Figs. 2(e) and 2(f)]. Close inspection of Fig. 2(d) shows that the interconnecting POT-rich regions are localized at depressed channels forming a network pattern through the PS-rich region [see arrows k in Figs. 2(d)–2(f)].

That POT-rich domains show up at depressed regions in the film may be due to the following factors. First, differences in the surface interactions of the two polymers result in differences in how well they wet the substrate. The thiophene group in the POT molecule should result in the more polar POT molecules next to the substrate. The POT-rich domains should therefore yield more uniform coverage resulting in overall smaller thickness on average.[21] Second, the difference of solubility of the two polymers in their common solvent can induce the topography dependence. During spin coating, solvent evaporates and demixing of PS and POT sets in. At an early stage the sample surface may be essentially smooth, apart from a small variation of the liquid surface by the different surface tensions of the PS- and the POT-rich phases. Owing to higher solubility of POT, the solvent in the PS-rich phase evaporates more, so that this phase solidifies earlier than the other phase. Subsequent evaporation of the remaining solvent leads to a further collapse of the better-soluble POT-rich phase. Finally, POT polymers change their conformation from aggregated chains to a more compact coiled shape when solvent is evaporated from the solution.[13] This conformational transition may result in lower topography of POT-rich domains as the molecules pack more closely as solvent evaporates.

Spin casting of a polymer solution involves fast drying of the solvent and produces thermodynamically unstable films deposited onto substrates. The process produces a relatively uniform coating of a blend quenched below its glass transition temperature, T_g. Annealing such films above T_g will cause the film to evolve toward thermal equilibrium according to dynamics involving interfacial interactions and surface-free energies of each polymer component in the blend. Domain growth and rearrangement accompanying significant restructuring of the components in the blends are expected upon annealing. We used NSOM for direct visualization of several intermediate steps of phase separation achieved by annealing the sample for specific time periods at various temperatures. The annealing temperatures were chosen as 120 °C, a temperature between the T_g of PS and POT, and 160 °C, above T_g of both PS and POT.

Typical NSOM results of the 2:1 blend samples annealed at 120 °C are displayed in Fig. 3. The morphology of 120 °C annealed samples changed significantly upon annealing. The roughness, the root-mean-square (rms) value in topographic z values of all the image pixels, increases as a result of annealing; 4 nm ± 2 nm in as-cast sample, 16 nm ± 4 nm in 15-min-annealed sample, and 17 nm ± 4 nm in 45-min-annealed sample. The images of annealed samples were obtained with the same NSOM tip. The pebbled surface seen in the topography of annealed samples is most likely a tip artifact. Different tip shapes will lead, for example, to different rms roughness measurements, where error bound represents standard deviation; it is therefore important to note that although the annealed samples were imaged with the same tip, the as-cast sample was imaged with a different tip. Results of topographic measurements on a sample annealed for 45 min show low-lying POT-rich domains that have shapes of round droplets with an average height of 6 nm ± 2 nm at the center and FWHM of 300–900 nm [see Fig. 3(d) and topographic profile]. These individual POT-rich droplets are then surrounded by elevated features rising up to 60 nm ± 15 nm from the lowest point in the topographic image [see arrows in Figs. 3(d)–3(f)]. Furthermore, the elevated domains, which are presumably derived from PS-rich regions that showed low fluorescence in the as-cast sample,

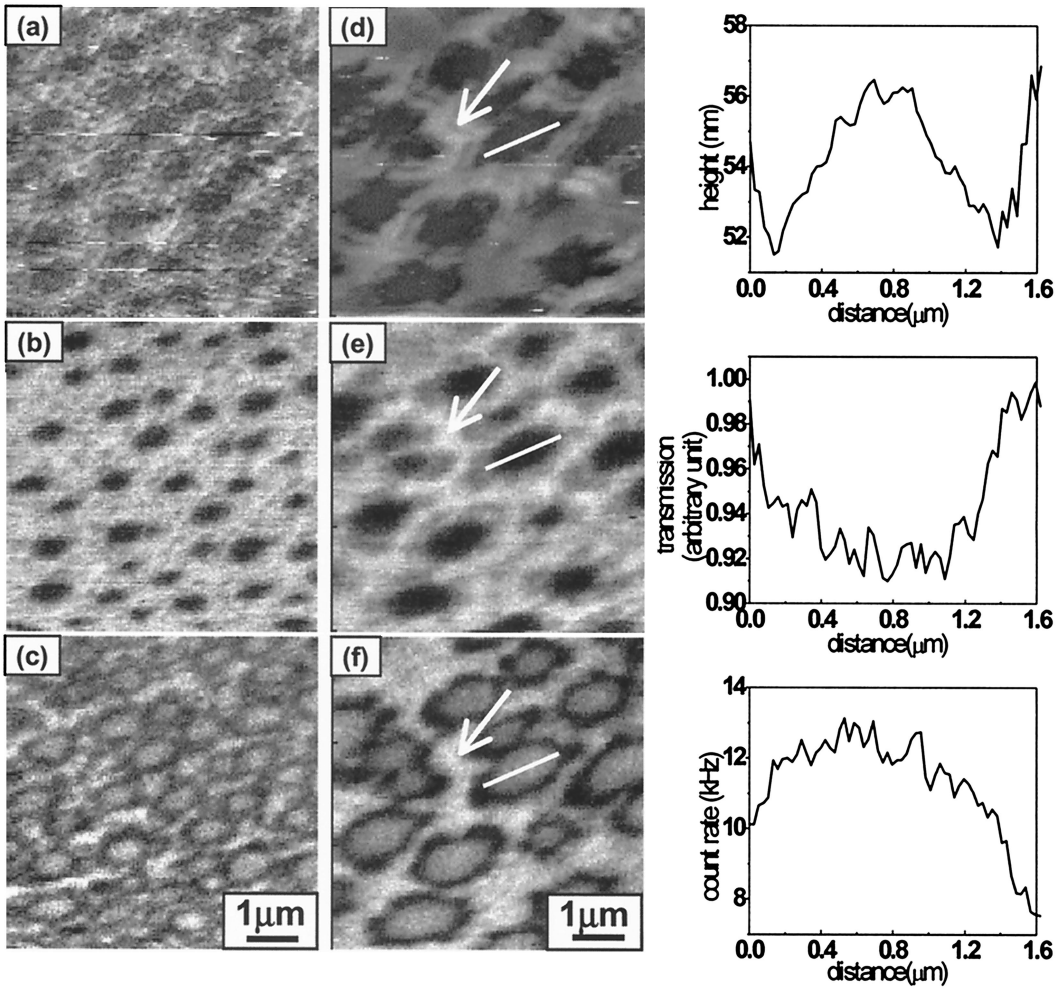

Fig. 3. Near-field images of annealed samples of PS:POT = 2:1 mixture cast at 314 rad/s (3000 rpm), and annealed at 120 °C for 15 min: (a) topography, (b) transmission, and (c) fluorescence. Images of a sample prepared in the same way but annealed for 45 min: (d) topography, (e) transmission, and (f) fluorescence. Values along the lines shown in (d)–(f) are shown to the right of these images. For the transmission plot the signal is normalized to 1 at the maximum along the line.

exhibited larger fluorescence signal both in intensity and in area as samples are annealed for longer times [Figs. 3(c) and 3(f)]. We believe that POT in the bulk of PS-rich phase further phase separated to diffuse to the surface of the PS-rich droplets from the bulk so that they can be more effectively excited with evanescent field of a NSOM probe. The evanescence field intensity decays exponentially away from the aperture with the form of $\exp[-z/f(a)]$ where z is distance from the aperture and $f(a) \approx a/1.5$, a characteristic length as a function of a, the aperture radius.[22] Therefore POT on the surface is excited with higher efficiency than the molecules in the bulk resulting in enhanced fluorescence signal. This would suggest that the POT is mobile even under the T_g of bulk POT when the molecules are cast with plasticizer, PS, with lower T_g. In addition, diffusion of POT molecules to the surface of the PS-rich regions is consistent with a lower surface free energy that is associated with POT.[21] Finally, these results are also consistent with secondary ion mass spectroscopy measurements acquired on the same polymeric system.[23]

NSOM results obtained on samples annealed at a higher temperature of 160 °C are displayed in Fig. 4. Upon annealing at 160 °C, above the T_g of both PS and POT, a more severe rearrangement of both polymer components was observed. The change in topography is clearly noticeable from the topography of the sample annealed for even a short time [Fig. 4(a)]. Topography obtained on a sample annealed for 10 min shows PS-rich domains separating into droplets. Although the topography changed, the optical images were similar to those for the as-cast samples. For samples annealed for slightly longer (15 min) we see evidence of vertical and lateral phase separation: The now larger droplets show brighter fluorescence [Fig. 4(f)], again suggesting a migration of POT to the surface of the PS-rich droplets.

Samples annealed for 45 min at 160 °C were similar to those annealed for 15 min at the same temperature. Topographic measurements show that

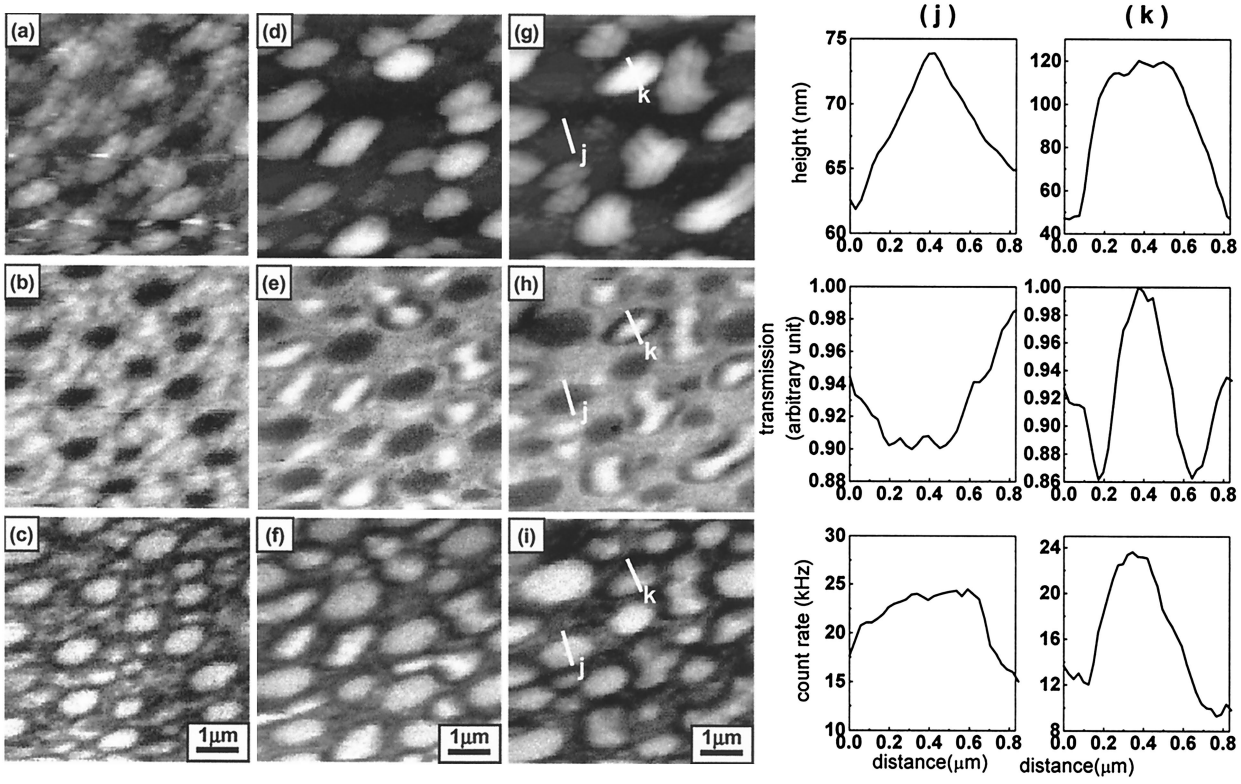

Fig. 4. Near-field images of annealed samples of PS:POT = 2:1 mixture cast at 314 rad/s (3000 rpm), and annealed at 160 °C for 10 min: (a) topography, (b) transmission, and (c) fluorescence. Images of a sample prepared in the same way but annealed for 15 min: (d) topography, (e) transmission, and (f) fluorescence. Images of a sample prepared in the same way but annealed for 45 min: (g) topography, (h) transmission, and (i) fluorescence. Values along the lines (j) and (k) are shown to the right. For the transmission plots the signal is normalized to 1 at the maximum along the line.

the fluorescent, POT-rich regions have grown into large droplets [compare Figs. 4(c) and 4(i)]. The aspect ratio (ratio of height to lateral dimension) of a typical POT-rich droplet is of order 10^{-2} (see topographic profile along line j in Fig. 4). PS-rich regions have evolved into highly elevated droplets with much larger aspect ratios of order 10^{-1} (topographic profile along line k in Fig. 4). Similar to the samples annealed at 120 °C, POT, with lower surface free energy, is expected to diffuse from bulk to the surface of the film. This was confirmed again from the fluorescence NSOM images seen as enhanced fluorescence signal at the surface of the high-rise droplets [Figs. 4(f) and 4(i)].

2D autocorrelation functions, calculated from topographic images, demonstrate the trend of roughening and growing of domains during the annealing process of the samples (Fig. 5). To obtain the curves in the lower part of the image, as described in the Section 2, we calculated the angle average of the height–height 2D autocorrelation function, $g(\boldsymbol{\xi}) = [\langle z(\mathbf{r})z(\mathbf{r} + \boldsymbol{\xi})\rangle - \langle z(\mathbf{r})\rangle^2]/\langle z(\mathbf{r})\rangle^2$ from the topographic images. The values were normalized against the maximum value at the origin of each image. The trend in domain sizes may be seen here as a trend in the widths of the autocorrelation functions. For the sample annealed at 120 °C the correlation function is significantly narrower for the 15-min-annealed sample, indicative of a decrease in the domain size as the PS-rich regions initially begin to breakup. For the sample annealed for 45 min the angle-averaged autocorrelation function decays more slowly, indicative of the increase in domain size visible in Fig. 3. Plots obtained from 160 °C annealed samples demonstrate a similar trend upon annealing.

For samples with large topography, artifacts due to interference effects or differences in tip–sample distance make image interpretation difficult in NSOM. For example, in the transmission images of Figs. 4(e) and 4(h), dark rings are clearly visible around otherwise bright regions that correspond to large droplets with heights as great as 72 nm. In a recent study[24] it was shown that thickness variations in thin films or droplets can give rise in NSOM to an interference effect similar to Newton's rings in ordinary optics. The transmission through the film will depend upon the local thickness that is due to multiple reflections from the film surfaces, i.e., the top surface of the sample and the surface between glass substrate and polymer sample. This effect tends to obscure near-field resolution in thin films by superimposing on the near-field transmission an additional signal with features determined by far-field interference effects. We suggest here that the rings seen in Figs. 4(e) and 4(h) are in fact far-field artifacts that are indicative of local thickness rather than lateral domain structure.

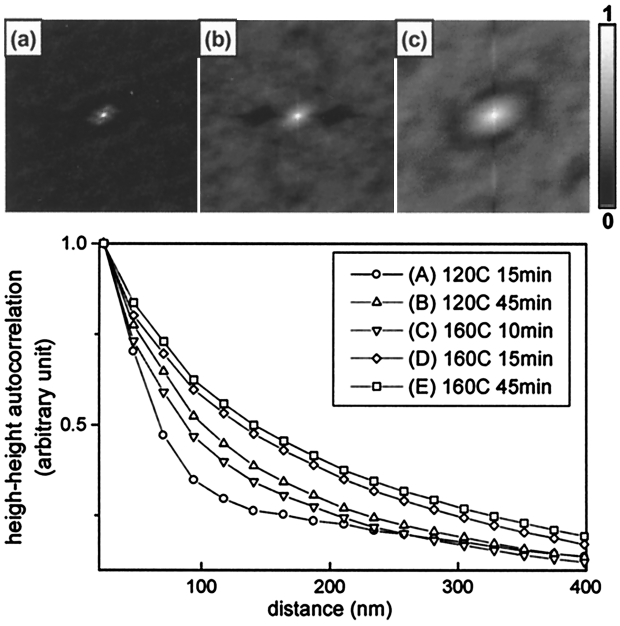

Fig. 5. Topographic 2D autocorrelation images and angle-averaged autocorrelation plots calculated from the topographic images. Images are for samples annealed (a) at 120 °C for 15 min, (b) at 160 °C for 10 min, (c) at 160 °C for 45 min. Image sizes are 6.7 μm × 6.7 μm.

In addition, we strongly suspect that the dark rings seen in fluorescence in Fig. 3(f) are also an artifact that is due to the sudden change in sample height at these domains (the dark regions correspond to a fluorescence count rate of 7.5 kHz, whereas the POT-rich domain has a 12.0-kHz peak count rate). NSOM tips are quite large; 200-nm-thick aluminum typically surrounds a fiber that tapers to an aperture that is approximately 100 nm in diameter, giving a tip that is 500 nm in diameter. As the surface of the film falls suddenly away at the edge of the POT-rich regions, the entire tip must clear the top before it can fall into the POT-rich valley. When the tip scans above the valley region, the tip aperture is therefore far from the surface for ~250 nm, approximately the width of these dark regions. Because of evanescent fields in the near field of the probe, changes in the height of the NSOM probe above a surface drastically change the tip–sample coupling and therefore also the detected signal.[22,25]

It is clear that, for large changes in topography, care has to be taken in interpretation of results that are due to induced artifacts. In Fig. 6 we show scatter plots of the fluorescence versus transmission signal obtained from NSOM images for each sample. We naïvely expect that, for a simple interpretation of the data, fluorescence and transmission should be anticorrelated; where the absorption is large, the fluorescence should be high. In the as-cast sample, which has a rms roughness of only 4 nm ± 2 nm, the scatter plot in fact shows good linear anticorrelation between transmission and fluorescence [Fig. 6(a)]. However, in the samples roughened by annealing, the distribution becomes more complicated as artifacts come into play [Figs. 6(b) and 6(c)]. If the scatter plots are reproduced with only the bottom 10 nm from each image, the anticorrelation is again recovered (Fig. 6 insets).

For better understanding of the topography effect on our optical images we used the fits in Fig. 6 in the following way. At each point in an image, the measured value of the transmission was subtracted from the transmission calculated from the fluorescence at that point and the appropriate fit of Fig. 6 (insets). The differences are shown in Fig. 7. The linear fit in all cases was obtained by performance of linear regression only with data points in the bottom 10 nm of the topography. To characterize the difference between the transmission image expected from the fit and the actual images, we calculate the rms deviations of the transmission data from the fit, and we divide these by the instrumental noise (similar to the chi square of a fit). The values are 1.91 for the as-cast sample; 2.72 and 3.39 for samples annealed at

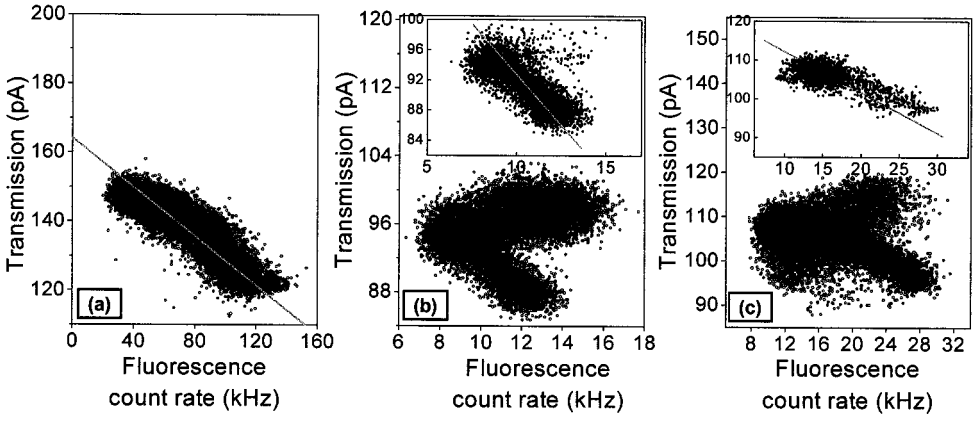

Fig. 6. Scatter plots of fluorescence versus transmission signal. All the samples are PS:POT = 2:1 blend cast at 314 rad/s (3000 rpm). (a) As cast, (b) sample annealed for 45 min at 120 °C, (c) sample annealed for 45 min at 160 °C. Insets, scatter plots and the best linear fit to the data points corresponding to the bottom 10 nm of topography. Figure (a) does not have an inset, since the overall range of the topography was 7.8 nm and the fit was performed to all the data points.

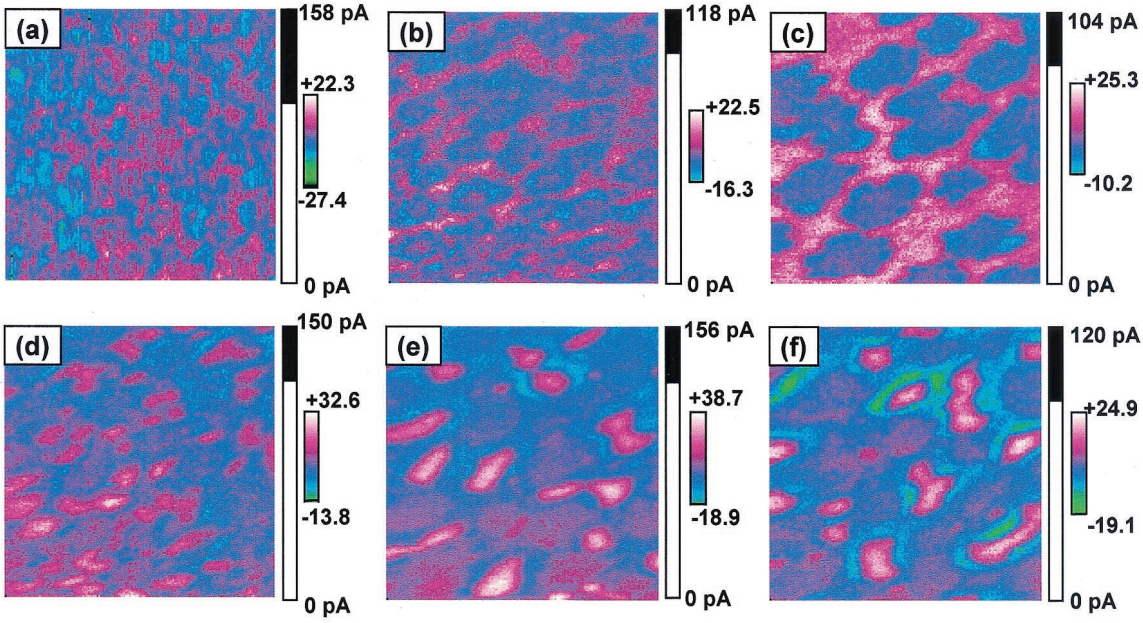

Fig. 7. Near-field correlation images calculated from transmission and fluorescence images for each sample. For every pixel the deviation of the transmission signal from the linear fit shown in Fig. 6 is plotted. Color scale bars are in picoamperes. The total range of transmission intensity for each image is shown as a black bar. The range of deviated signal was rescaled into 256 level so that each intensity value is assigned with a color in the color table shown in each image. All the samples are PS:POT = 2:1 mixture cast at 314 rad/s (3000 rpm). (a) As-cast, (b) annealed for 15 min at 120 °C, (c) annealed for 45 min at 120 °C, (d) annealed for 10 min at 160 °C, (e) annealed for 15 min at 160 °C, (f) annealed for 45 min at 160 °C.

120 °C for 15 and 45 min, respectively; 4.21, 5.70, and 6.21 for samples annealed at 160 °C for 10, 15, and 45 min, respectively. The results demonstrate that the degree of deviation increases as the annealing temperature and time increase, concomitantly as the rms of the z-height values from topography images increases. The images in Fig. 7, when they are compared with topographic information, clearly show that the regions exhibiting anomalous transmission signal correspond to the regions with significant roughness. For instance, in the 120 °C annealed sample, comparison between Fig. 7(c) and Fig. 3(d) reveals that the transmission signal is enhanced as the NSOM probe scans over the thicker region of the sample. This artifact appears to be more significant on the samples annealed at higher temperature; the scatter plots in Fig. 6(c) include noncorrelating points located above [enhanced transmission, correspond to points seen as pink to white colors in Fig. 7(f)] the fitted line and below [suppressed transmission, blue to green colors in Fig. 7(f)] as well. By comparison with the corresponding topographic image, the enhancement and suppression of the transmission signal are shown from the top thickest regions and from steep edges of the highly elevated domains, respectively. More quantitative measurements and modeling of these transmission anomalies are discussed in detail elsewhere.[24]

4. Conclusions

In summary, we have presented data and qualitative analysis of the phase-separation dynamics of thin-film blends of poly(styrene) (PS) and poly(3-octylthiophene) (POT), using near-field scanning optical microscopy. Our home-built near-field microscopes were used to image domains in polymer blend films with a resolution beyond the diffraction limit of conventional optics. Simultaneous topography, transmission, and fluorescence NSOM images taken on these samples at different annealing stages revealed details of phase separation, such as the existence of a percolating network of POT, that are not observable by other techniques. Some artifacts in NSOM measurement were identified with the aid of simultaneously obtained fluorescence and topographic information. Recent research on film thickness and topographic artifacts in transmission NSOM has been of some help in understanding these effects; however, further modeling is necessary for a quantitative analysis of transmission data and for a better understanding of the fluorescence data on rough samples.

The authors thank John Dagata, Lipiin Sung, Lee Richter, Jack Douglas, and Ken Weston for helpful discussions. This research was supported by the Advance Technology Program of the National Institute of Standards and Technology (NIST) and the NIST Director's competence program. Certain commercial equipment, instruments, or materials are identified in this paper to foster understanding. Such identification does not imply recommendations or endorsements by NIST, nor does it imply that the materials or equipment identified are necessarily the best available for the purpose.

References and Notes

1. A. Karim, J. F. Douglas, B. P. Lee, S. C. Glotzer, J. A. Rogers, R. J. Jackman, E. J. Amis, and G. M. Whitesides, "Phase separation of ultrathin polymer-blend films on patterned substrates," Phys. Rev. E **57,** R6273–R6276 (1998).
2. B. D. Ermi, A. G. Nisato, J. F. Douglas, J. A. Rogers, and A. Karim, "Coupling between phase separtion and surface deformation modes in self-organizing polymer blend films," Phys. Rev. Lett. **81,** 3900–3903 (1998).
3. A. Karim, T. M. Slawecki, S. K. Kumar, J. F. Douglas, S. K. Satija, C. C. Han, T. P. Russel, Y. Liu, R. Overney, J. Sokolov, and M. H. Rafailovich, "Phase-separation-induced surface patterns in thin polymer blend," Macromolecules **31,** 857–862 (1998).
4. B. D. Ermi, A. Karim, and J. F. Douglas, "Formation and dissolution of phase-separated structures in ultrathin blend films," J. Polym. Sci. B **36,** 191–199 (1998).
5. H. Nishino, G. Yu, A. J. Heeger, T.-A. Chen, and R. D. Rieke, "Electroluminescence from blend films of poly(3-hexylthiophene) and poly(N-vinylcarbazole)," Synth. Met. **68,** 243–247 (1995).
6. D. W. Pohl, W. Denk, and M. Lanz, "Optical stethoscopy: image recording with resolution $\lambda/20$," Appl. Phys. Lett. **44,** 651–653 (1984).
7. E. Betzig, J. K. Trautman, T. D. Harris, J. S. Weiner, and R. L. Kostelak, "Breaking the diffraction barrier: optical microscopy on a nanometric scale," Science **251,** 1468–1470 (1991).
8. J. W. Blatchford, T. L. Gustafson, A. J. Epstein, D. A. Vanden Bout, J. Kerimo, D. A. Higgins, P. F. Barbara, D.-K. Fu, T. M. Swager, and A. G. MacDiarmid, "Spatially and temporally resolved emission from aggregates in conjugated polymers," Phys. Rev. B. **54,** R3683–R3686 (1996).
9. J. A. DeAro, K. D. Weston, S. K. Burrato, and U. Lemmer, "Mesoscale optical properties of conjugated polymers probed by near-field scanning optical microscopy," Chem. Phys. Lett. **277,** 532–538 (1997).
10. L. A. Nagahara, M. Nakamura, and H. Tokumoto, "Investigation of mesoscopic domains in thin organic films using near-field optical absorption mapping," Ultramicroscopy **71,** 281–285 (1998).
11. T. Shiga, T. Narita, K. Tachi, A. Okada, H. Takahashi, and T. Kurauchi, "Measurement of internal stresses in coating using time resolved fluorescence," Polym. Eng. Sci. **37,** 24–30 (1997).
12. According to ISO 31-8, the term, "molecular weight" has been replaced with "relative molecular mass," M_W. The conventional notation, rather than the ISO notation, has been employed for this publication.
13. G. W. Heffner, D. S. Pearson, and C. L. Gettinger, "Characterization of poly(3-octylthiophene). I. Molecular characterization in dilute solution," Polym. Eng. Sci. **35,** 860–867 (1995).
14. E. Betzig, P. L. Finn, and J. S. Weiner, "Combined shear force and near-field scanning optical microscopy," Appl. Phys. Lett. **60,** 2484–2486 (1992).
15. J. Barenz, O. Hollricher, and O. Marti, "An easy-to-use non-optical shear-force distance control for near-field optical microscope," Rev. Sci. Instrum. **67,** 1912–1916 (1996).
16. P. Derose, J. Hwang, and L. S. Goldner, "Near-field scanning optical microscopy for imaging domains in biomembranes," in *Laser Techniques for Surface Science III,* H. Dai and H. Freund, eds., Proc. SPIE **3272,** 93–98 (1998).
17. L. Gheber, J. Hwang, and M. Edidin, "Design and optimization of a near-field scanning optical microscope for imaging biological samples in liquid," Appl. Opt. **37,** 3574–3581 (1998).
18. W. H. Press, S. A. Teukolsky, W. T. Vetterling, and B. P. Flannery, in *Numerical Recipes in C*, 2nd ed. (Cambridge, New York, 1992), pp. 496–502.
19. D. B. Hall, P. Underhill, and J. K. Torkelson, "Spin coating of thin and ultrathin polymer fims," Polym. Eng. Sci. **38,** 2039–2045 (1998).
20. L. Sung, A. Karim, J. F. Douglas, and C. C. Han, "Dimensional crossover in the phase separation kinetics of thin polymer blend fims," Phys. Rev. Lett. **76,** 4368–4371 (1996).
21. M. Boltau, S. Walheim, J. Mlynek, G. Krausch, and U. Steiner, "Surface-induced structure formation of polymer blends on patterned substrates," Nature (London) **391,** 877–879 (1998).
22. C. E. Jordan, S. J. Stranick, R. R. Cavanagh, L. J. Richter, and D. B. Chase, "Near-field scanning optical microscopy incorporating Raman scattering for vibrational mode contrast," Surf. Sci. **433–435,** 48–52 (1999).
23. Unpublished measurements by Greg Gillen and John Dagata at the National Institute of Standards and Technology, Gaithersburg, Maryland 20899.
24. L. Goldner, J. Hwang, G. W. Bryant, M. Fasolka, P. P. Absil, J. V. Hryniewicz, F. G. Johnson, H. Shen, and P.-T. Ho, "Newton's rings in near-field optics," Appl. Phys. Lett. **78,** 583–585 (2001).
25. E. Betzig, A. Harootunian, A. Lewis, and M. Isaacson, "Near-field diffraction by a slit: implications for superresolution microscopy," Appl. Opt. **25,** 1890–1900 (1986).